NANO · MICRO small
www.small-journal.com

Electrochemically Dealloyed 3D Porous Copper Nanostructure as Anode Current Collector of Li-Metal Batteries

*Yifan Ma, Xuetian Ma, Jianming Bai, Wenqian Xu, Hui Zhong, Zhantao Liu, Shan Xiong, Lufeng Yang, and Hailong Chen**

The commercialization of high-energy Li-metal batteries is impeded by Li dendrites formed during electrochemical cycling and the safety hazards it causes. Here, a novel porous copper current collector that can effectively mitigate the dendritic growth of Li is reported. This porous Cu foil is fabricated via a simple two-step electrochemical process, where Cu-Zn alloy is electrodeposited on commercial copper foil and then Zn is electrochemically dissolved to form a 3D porous structure of Cu. The 3D porous Cu layers on average have a thickness of ≈14 um and porosity of ≈72%. This current collector can effectively suppress Li dendrites in cells cycled with a high areal capacity of 10 mAh cm^{-2} and under a high current density of 10 mA cm^{-2}. This electrochemical fabrication method is facile and scalable for mass production. Results of advanced in situ synchrotron X-ray diffraction reveal the phase evolution of the electrochemical deposition and dealloying processes.

1. Introduction

Li metal anode is under the spotlight of multiple Li-chemistry-based electrochemical energy storage technologies, as it has the highest theoretical capacity (3860 mAh g^{-1}) and lowest electrochemical potential (−3.04 V vs standard hydrogen electrode) compared with other anodes.[1] Over the past few decades, Li-ion batteries (LIBs) have played critical roles in many important applications.[2] The mobile network and electrified transportation have been largely relying on the development of LIBs.[3] However, the energy density of conventional commercial LIBs with graphite anode is approaching its upper limit. Li metal anode seems to be the most promising means to further increase the energy density.[4] However, a number of remaining challenges must be addressed for the commercialization of Li metal anodes: 1) undesired dendritic growth of Li can penetrate the separator and cause internal short-circuit, resulting in severe safety hazards;[5–7] 2) the irreversible parasitic reactions between Li and electrolyte can form thick solid electrolyte interphase (SEI) layer on the surface of Li metal, consuming Li and electrolyte, increasing internal resistance, and thus shortening cycling life;[8] 3) during the processes of repeated Li plating and stripping, Li anode has large volumetric and morphological changes. But the SEI layer is too fragile to accommodate such significant changes, thus resulting in continuous Li loss in forming new SEI.[9] And 4) stripping of Li is more likely to start from the root of the dendrites, causing Li pieces falling off and losing electric connection, thus resulting in so-called "dead Li" and low Coulombic efficiency.[10,11] Stabilization of Li-metal anode is the key to enable Li-metal batteries. In recent years, tremendous efforts have been made to address the challenges regarding suppression of Li dendrite and stabilization of SEI, including 1) electrolyte engineering;[10,12–14] 2) interfacial engineering;[15–18] 3) use of solid electrolyte,[19–23] and 4) use of 3D structured current collectors.[24–37] All of these strategies have shown their positive influence on suppressing Li dendrite growth and led to improved electrochemical performances to different extents. Among these approaches, the use of 3D-structured current collectors showed high promise and the advantages in cost. Compared to flat foil current collectors, 3D-structured current collectors have much larger active surface area, providing a larger Li/electrolyte interface, thus can reduce the practical current density and lower the possibility of stimulating dendritic growth.[24] Many previous reports have demonstrated that 3D current collectors can effectively suppress Li dendrite growth, such as rimous Cu foam,[38] CuO nanowire array,[39] dendritic copper current collectors,[26] N-doped carbon rod array,[40] graphitized carbon fibers,[41] vertically aligned CuO nanosheets,[42] crumbled graphene balls,[31] Cu–CuO–Ni Hybrid Structure,[33]

Y. Ma, X. Ma, Z. Liu, S. Xiong, L. Yang, H. Chen
The Woodruff School of Mechanical Engineering
Georgia Institute of Technology
Atlanta, GA 30332, USA
E-mail: hailong.chen@me.gatech.edu
J. Bai, H. Zhong
National Synchrotron Light Source II
Brookhaven National Laboratory
Upton, NY 11973, USA
W. Xu
X-ray Science Division
Advanced Photon Source
Argonne National Laboratory
Lemont, IL 60439, USA

The ORCID identification number(s) for the author(s) of this article can be found under https://doi.org/10.1002/smll.202301731

DOI: 10.1002/smll.202301731

cellular Cu@CuO composite,[43] wettable carbon felt framework,[27] and vertically grown edge-rich graphene nanosheets.[44] Luo et al. conducted phase field simulation to track the Li morphology evolution on different current collectors, and demonstrated that 3D current collector can help suppress Li dendrite growth and promote Li metal deposition by homogenizing Li^+ flux.[45,46] However, many of these methods are sophisticated with multiple steps and were only demonstrated in small scales such as in coin cells. The scale-up of these methods can be difficult and high-cost. It would be particularly difficult to integrate most of these methods into the roll-to-roll manufacturing process predominately used in current LIBs industry, which requires not only facile processing steps, but also good mechanical strength of the current collector materials. Most aforementioned carbon and metal nanostructures are not mechanically strong enough and they have to be applied on conventional Cu current collectors, which substantially lowers the overall energy density and hedges their advantages.

As an alternative approach, in our previous work,[47] we used a one-step electrodeposition method to fabricate 3D porous Cu current collectors directly on commercial Cu foil. This new current collector can offer an areal capacity as high as 4 mAh cm^{-2} with no Li dendrite growth in long term cycling. Because this method is simple and facile and does not require expensive facility or multiple processing steps, in principle it can be directly integrated into the roll-to-roll production, presenting a significant advantage in commercialization. However, in previous work, obtaining thick, porous Cu deposition layer remains to be a challenge. The optimal thickness was only ≈5 um with porosity of ≈76%. If keeping increasing the deposition thickness, the porosity becomes lower, resulting in loss of overall areal capacity. Therefore, to clear the roadblock of this current collector towards commercialization, preparation of 3D porous layers with high thickness and reasonable porosity is the key. Previous studies by Yun et al.[48] and Zhao et al.[34] have utilized chemical/electrochemical methods to etch commercial brass and fabricate 3D porous Cu, which demonstrated good electrochemical performances. Recently, we raised a new strategy to obtain thick, porous layer of Cu with using a two-step electrochemical process: we first electrodeposit a very thick Cu-Zn alloy layer and then electrochemically dealloy it to remove Zn and leave a highly porous 3D Cu nanostructure. In our work, the Cu-Zn alloy is directly deposited on commercial Cu foil. Thus, the thickness and the porosity of the dealloyed porous layer are tunable by tuning the thickness of the deposited Cu-Zn layer and by tuning the Zn/Cu ration (e.g., higher Zn fraction results in higher porosity). The 3D porous Cu layers on average have a much higher thickness of ≈14 um and a porosity of ≈72%. This new 3D Cu current collector demonstrated stable Li plating/stripping at an areal capacity of 10 mAh cm^{-2} at current density of 10 mA cm^{-2} up to 230 h, showing high promise of its applications in Li metal batteries.

2. Results and Discussion

As mentioned in Introduction, the thickness of porous Cu from direct one-step electrodeposition is limited. The pores would be jammed as the deposition time increases in a variety of deposition conditions that we have tried.[47] Here we took a different approach by depositing Cu and Zn together and then electrochemically dissolve Zn, making use of the significant difference in the standard electrode potentials of Cu and Zn. It is expected that the removal of Zn can leave a more porous structure of Cu, while the total thickness is not limited, solely depending on the thickness of the deposited Cu-Zn alloy layer. In the deposition process, Cu-Zn alloy was deposited on the surface of commercial copper foil in galvanostatic mode. It was found that many factors can affect the composition, phase, and morphology of the deposited layer. The ratio of total Cu and Zn deposited is strongly influenced by the ratio of Cu and Zn salts in the electrolyte, also less significantly influenced by the deposition current. This is because the electrode potential of Cu is 1.107 V higher than that of Zn and thus Cu tends to be deposited first. In a slow and close-to-equilibrium deposition condition, Cu and Zn would deposit as simple metals in order. While in a fast deposition with Zn concentration being much higher than that of Cu, the kinetic factor can result in the co-deposition of Cn-Zn alloy. In this work, we optimized the Cu:Zn ratio in the electrolyte to be 0.06:1, in order to achieve a Cu-poor composition in the deposited layer, with the expectation that such composition can cause more Zn removal and result in higher porosity of the remaining Cu. By optimizing the current density and electrolyte concentration, Cu-Zn alloy with desired phase, density, and thickness was obtained. The red line in **Figure 1**a shows the XRD pattern of as-deposited Cu-Zn alloy. The main phase was indexed as $CuZn_5$, a Zn-rich alloy phase, and the minor phase was identified as Cu_5Zn_8, a relatively Cu-rich phase. Figure 1b shows the SEM image of the deposited Cu-Zn alloy. The particle size ranges from 1 to 8 μm and the film is quite uniform and dense. With the deposition time of 1 h, the typical thickness is 13–15 μm.

The electrochemical dealloying process was conducted in 0.2 M NaCl electrolyte with a Ni foam counter electrode. Potentiostatic mode was used instead of galvanostatic mode and the applied voltage was set between the oxidation potentials of Zn and Cu, which ensures that only Zn is oxidized and dissolved but not Cu. The current profile during dealloying process was shown in Figure S1 (Supporting Information). The black line in Figure 1a shows the XRD pattern of a sample after 3 h dealloying under a voltage of 0.4 V (vs Ni foam). After dealloying, Bragg peaks of $CuZn_5$ phase are gone and a small amount of Cu_5Zn_8 can still be seen. The signal from the remaining Cu and the Cu substrate superposes at the same two-theta positions. Noticeably, the 3D Cu layer after dealloying shows high (220) peak intensity, suggesting it is textured. This may result from the texture of the deposited Cu-Zn alloy. Similar phenomenon is also observed by Shan et al. in previous work.[49] Figure 1c,d shows the SEM images of surface of the sample after dealloying. The dense, solid particles seen in Figure 1b now becomes a very porous structure with thin walls of ≈40 nm. A thin layer of Cu_2O was detected by XPS (Figure S2, Supporting Information) on the surface of 3D porous Cu. This thin layer of Cu_2O has higher lithiophilicity and can help regulate uniform Li nucleation and plating on the 3D Cu structure.[50] The porosity of the 3D porous Cu layer was estimated to be ≈72% (the detailed calculation can be found in the Supporting Information), which is similar to that of the directly deposited 3D Cu current collector in our previous work (70–76%). However, it should be noted that the thickness of this sample is much higher, ≈14 um, while the upper limit of the thickness of directly deposited Cu with the similar porosity is ≈5 um. Therefore, roughly 3 times

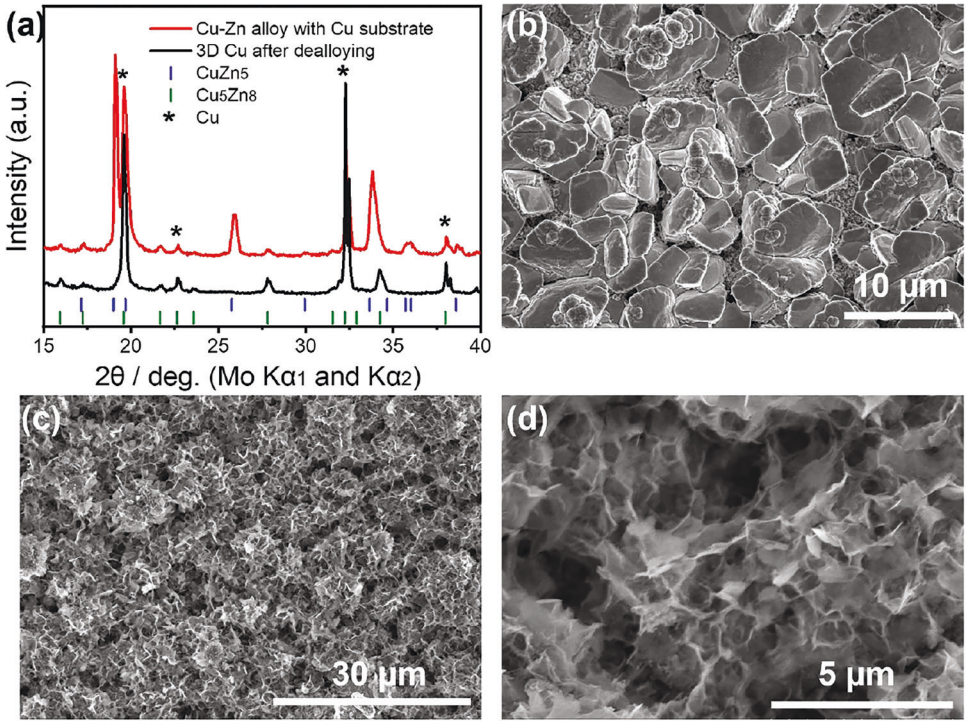

Figure 1. a) XRD patterns of deposited Cu-Zn alloy and 3D Cu after dealloying b) SEM of deposited Cu-Zn alloy c) SEM of 3D Cu after dealloying and its zoom-in view (d).

more pore space is created in this new 3D Cu current collector, which definitely helps to improve the areal Li storage capacity. It is observed that despite the deposition thickness is much higher, the adhesion to the commercial copper foil is still very strong. Therefore, in principle it can be directly used as current collectors in the roll-to-roll process.

The ex situ XRD results showed that the phase evolution in the deposition and dealloying processes is not simple. It involves at least 3 phases ($CuZn_5$, Cu_5Zn_8, and Cu) and possibly more phases in the intermediate steps. In order to further understand the full phase evolution pathway, so to optimize the deposition/dealloying processes and possibly rationally tune the electrochemical performance in the future, in situ XRD observation is critically desired. We designed a unique in situ XRD platform and successfully used it to realize in situ XRD data collection for both the deposition and dealloying processes at multiple synchrotron beamlines (see Experimental Section for details). The in situ platform is also a two-electrode system with using the same electrodes as used in laboratory. Same electrolyte concentration and controlled current or voltage were used. **Figure 2** shows the in situ XRD patterns of the deposition (a) and dealloying (c) processes, and the corresponding quantitative analysis in (b) and (d), respectively. In the deposition process, it can be seen that $CuZn_5$ phase starts growing at the very beginning of the deposition, implying it might be the most stable phase under this certain electrolyte concentration and overpotential. Towards the end of the deposition, pure Zn phase is observed, which was not observed in the ex situ experiments. This is likely because the volume of the in situ cell is much smaller (8 ml) than the volume of the beaker (100 ml) used in the ex situ experiments and Cu salt depletes. In the dealloying process, as expected, Zn and $CuZn_5$ phase quickly lowers its peak intensity. Yet, to our surprise, Cu_5Zn_8 phase gradually formed after 5 min and it did not disappear at the very end after 40 min. This implies that the dealloying of $CuZn_5$ is not as simple as just dissolution/removal of Zn. Rather, Cu_5Zn_8 may function as an intermediate phase and it maintained an equilibrium with pure Cu as the final product, as illustrated in the reaction below.

$$Zn \rightarrow Zn^{2+}$$

$$CuZn_5 \rightarrow Cu_5Zn_8 \Leftrightarrow Cu \quad (1)$$

More importantly, with the high resolution of synchrotron XRD, the deposition/dealloying processes can be precisely quantified with using integration of peak intensities. In Figure 2b, peak intensities are integrated for (103) peak (≈9.14 degree) for $CuZn_5$ phase and (102) peak (≈6.62 degree) for Zn phase. Very clearly both integrations increase linearly as a function of time, agreeing very well with the fact that this is a galvanostatic experiment and the Coulombic flow is a linear function of time. Figure 2d shows the integration of selected peaks of $CuZn_5$ and Zn during dealloying process. In the first 5 min, Zn is quickly leached and gone. While at the same period of time, the intensity of $CuZn_5$ phase stays the same, showing that the corrosion/dissolution strongly favors Zn, which essentially functions here as a sacrificial anode. After Zn is gone, the intensity of $CuZn_5$ starts to drop in 5–15 min. The corrosion rate lowers down after 15 min and finally the peak completely disappeared after 20 min. Meanwhile, peaks of Cu_5Zn_8 show up after 5 min, exactly the same time when $CuZn_5$ begins the dealloying process.

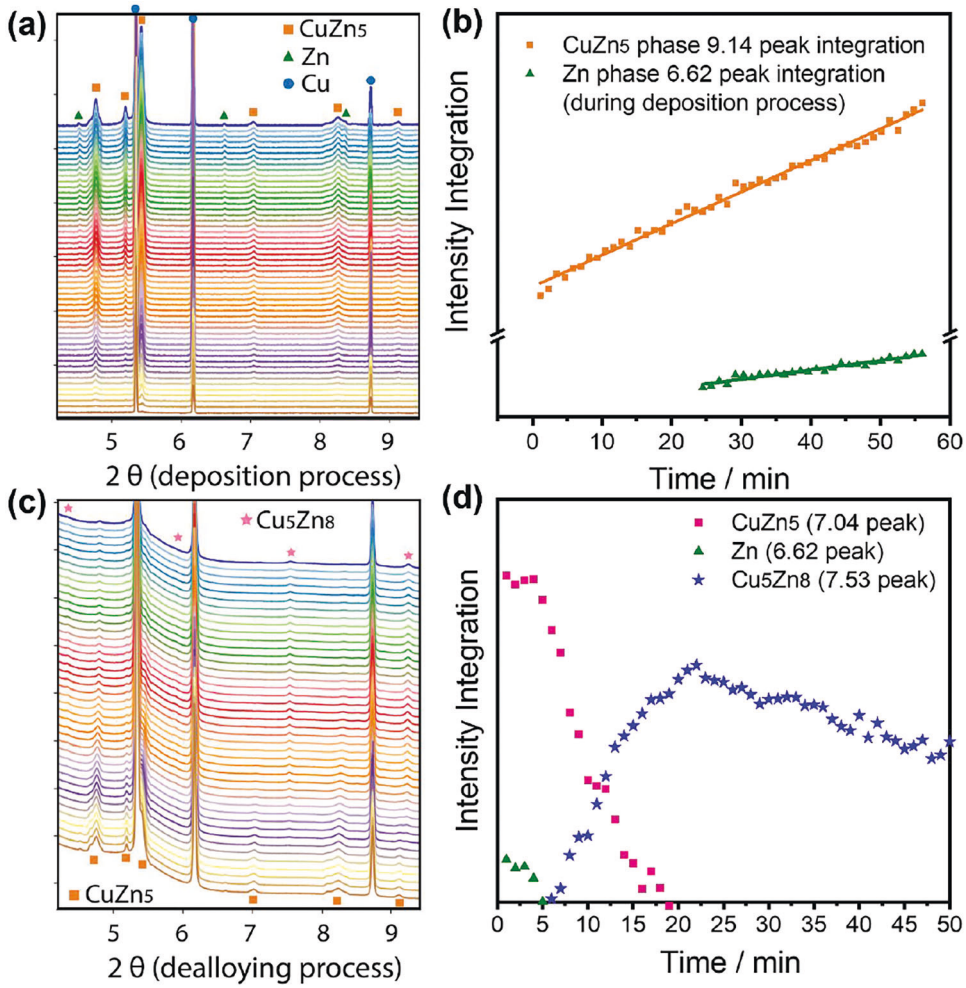

Figure 2. In situ XRD patterns (scan rate 1 pattern per min) during deposition a) and dealloying process of Cu-Zn alloy (c), and their corresponding selected peak intensity integration (b,d).

After that, peak intensities of Cu_5Zn_8 gradually increase from 6–22 min, along with decrease of peak intensities of $CuZn_5$ phase, indicating the phase transformation from $CuZn_5$ to Cu_5Zn_8. At ≈20 min, $CuZn_5$ is fully dealloyed and correspondingly, peak intensities of Cu_5Zn_8 stop increasing, beginning transformation from Cu_5Zn_8 to Cu, evident by a gradually decreasing intensity. The quantification of formed Cu phase, however, was not conducted due to the overlapping of the signals from the Cu substrate.

The electrochemical performance of this 3D Cu sample as current collector in Li metal batteries is evaluated first in Li//Li@3D Cu half cells, which used Li foil as the counter/reference electrode and 3D Cu as the working electrode. Similar cells were also assembled with using commercial Cu foil as the working electrode as the control experiment. **Figure 3**a shows the voltage profiles of cells cycled with areal capacity of 1 mAh cm^{-2} at a current density of 1 mA cm^{-2}. In the 1st cycle, 2 mAh cm^{-2} of Li is plated onto the 3D Cu current collector to provide sufficient Li in following cycles. Voltage profiles of 3D Cu show no spikes or large voltage fluctuations up to 350 h, indicating good cycling stability. As a comparison, the cell with commercial Cu foil showed large voltage fluctuations and spikes in very early stage of cycling, implying the growth of dendritic Li, and the cell completely failed after 150 h. Zoomed-in voltage profiles from 110 to 120 h cycles are shown in Figure 3b. Cells with commercial Cu foil as current collector have unstable voltage oscillations and spikes during Li plating/stripping process, which may result from heterogeneous SEI formation and soft-shorting caused by Li dendrites. In comparison, cells with 3D Cu have a stable voltage amplitude as low as 30 mV, indicating low internal resistance and excellent ionic and electronic conduction, which can be attributed to uniform SEI and stable structure of 3D Cu. Voltage profiles of cells tested with a larger areal capacity are shown in Figure 3c,d. In this test, 15 mAh cm^{-2} of Li is plated onto 3D Cu current collector to provide sufficient Li in following cycles. Even at an areal capacity as large as 10 mAh cm^{-2} (current density 10 mA cm^{-2}), cells with 3D Cu as current collector can still deliver good cycling stability up to 230 h. Columbic efficiency (CE) of half cells using 3D Cu and commercial Cu foils as current collectors are shown in Figure S4 (Supporting Information). Half cell with 3D Cu shows higher and more stable Columbic efficiency than that of commercial Cu foil. The voltage profiles during the first Li deposition process of

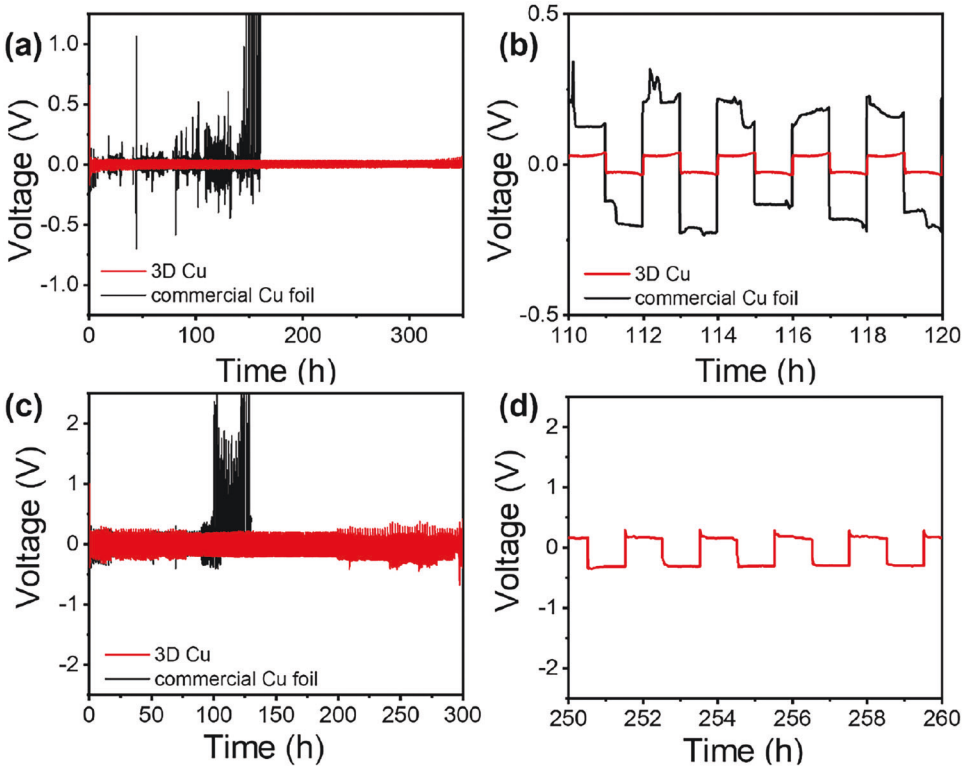

Figure 3. Voltage profiles of Li plating/stripping of 3D Cu and commercial Cu foil cells at a) 1 mAh cm^{-2} and c) 10 mAh cm^{-2}, respectively. b) The detailed voltage profiles from 110 h to 120 h in (a). d) The detailed voltage profiles from 200 h to 220 h cycle in (c).

these half cells are plotted in Figure S5 (Supporting Information). Half cell with 3D Cu shows a much lower Li nucleation overpotential than that of commercial Cu foil, demonstrating the 3D Cu current collector can provide more Li nucleation sites and lower the Lu nucleation barrier. The superior Li-storage capability of the 3D current collectors can be ascribed to both large thickness and high porosity, as well as large active surface area and hierarchical pore structures, demonstrating its promise for applications as current collectors in Li metal batteries. It can be used in cells with conventional liquid electrolytes, as demonstrated in this work, and perhaps in solid state cells too.[51,52]

Figure 4 shows the morphology evolution of 3D current collectors after Li plating (1, 4, 10 mAh cm^{-2}) and stripping (until cell voltage > 0.5 V) at different areal capacities. After depositing 1 mAh cm^{-2} Li, the top view of the 3D current collector (Figure 4a) becomes very different from the pristine (Figure 1d). It becomes much denser from the cross-section view (Figure 4d) and the pores are not seen in the top view (Figure 4a), indicating Li is deposited into the 3D current collector and filled the pores. Besides, there are also sphere Li particles seen on surface, suggesting Li is deposited both into the pores and on surface. After stripping of Li (Figure 4g), a porous structure is seen but slightly different from the pristine (Figure 1d) in that the walls become thicker, which likely is the SEI layer formed on the surface of Cu. When depositing more Li (4 and 10 mAh cm^{-2}), the surface of the 3D current collector is covered by Li particles, as the porous structure cannot completely accommodate such amount of Li. The deposited Li possesses a granular shape and forms a relatively flat and smooth surface, with no dendrites seen. This can be attributed to the large surface area of the 3D Cu structure providing high density of nucleation sites for Li. In such condition, very unlikely Li would deposit on a few hot spots to form dendrites. After plating and stripping 4 and 10 mAh cm^{-2} Li, an interconnecting porous structure is seen, which might be remained SEI layer. The composition of the SEI layer after cycling was investigated by XPS (Figure S7, Supporting Information). The main components of the SEI layer consist of LiF, R-OLi, LiN_xO_y, and other solvent/LiTFSI degradation products, which is similar to what is expected from previous reports which used the same or similar electrolytes.[53,54] In addition, from cross section views of the 3D Cu current collector, it can be clearly seen that its 3D porous structure is well maintained after Li plating/stripping. The SEM results demonstrate that the porous 3D Cu current collector can provide rich Li nucleation sites, facilitate flat, dense, and homogenous deposition of Li and effectively suppress Li dendrite growth.

To explore the potential of using the 3D porous Cu current collectors in practical applications, full cells with using Li@3D Cu as the anode and commercial $LiFePO_4$ as the cathode were assembled. One mAh cm^{-2} of Li was first plated onto the 3D Cu current collector using symmetric cells. Then the lithiated current collectors were taken out and used as anode in full cells. The cycling performance of the assembled full cells was tested in a voltage window of 2.0–4.2 V at 1 C rate. For comparison, full cells with using Li@commercial Cu foil as anode were also assembled and tested with same conditions. **Figure 5**a shows the 1st charge/discharge curves of the full cells using 3D and commercial Cu foil current collectors. The cell using 3D Cu delivers an initial discharge capacity of 142.0 mAh g^{-1}, which is nearly

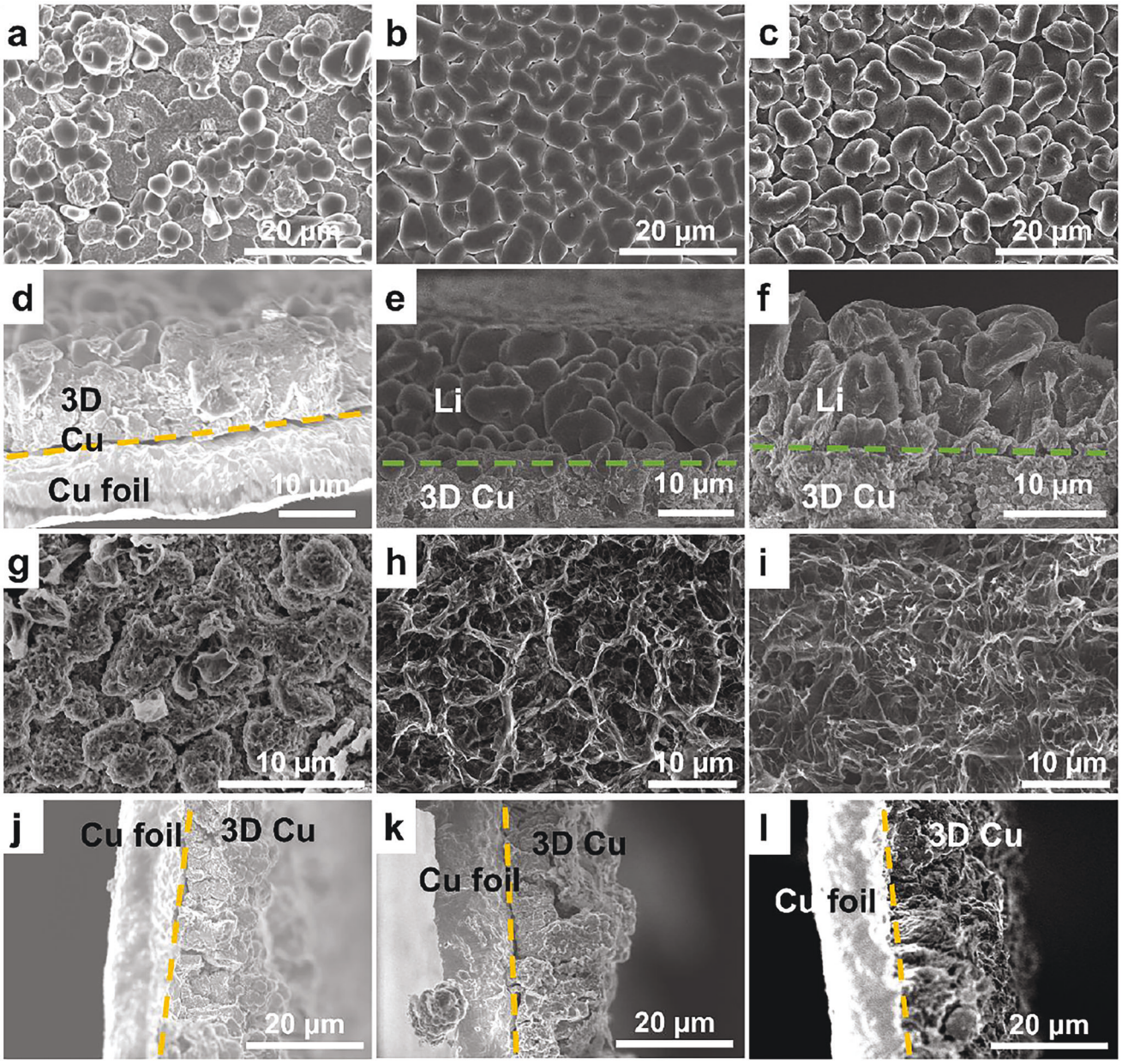

Figure 4. SEM images of 3D current collectors after Li plating/stripping. Top view images of 3D Cu current collector after Li plating of a) 1 mAh cm^{-2}, b) 4 mAh cm^{-2}, c) 10 mAh cm^{-2}, and corresponding cross sections (d,e,f). The yellow dotted lines denote the boundaries between Li (top) and deposited 3D porous Cu (bottom). Top view images of 3D current collector after Li stripping of g) 1 mAh cm^{-2}, h) 4 mAh cm^{-2}, i) 10 mAh cm^{-2}, and corresponding cross sections (j,k,l).

the same as the cell using commercial Cu foil. Figure 5b shows the charge/discharge curves of full cell using 3D Cu anode in the 1st, 2nd, and 10th cycles at 1C. The capacity loss between 1st and 2nd cycle may result from irreversible Li consumption due to SEI formation. During the initial 100 cycles (as shown in Figure 5c), the cell with 3D Cu presents a slight capacity decay from 142.0 to 117.3 mAh g^{-1} with a capacity retention of 82.6%. The commercial Cu cells failed after 40 cycles, likely due to the short-circuit caused by the formation and growth of Li dendrites. While the 3D Cu current collector allows for longer cycling as it mitigates the growth of Li dendrite much better than the flat commercial Cu foil. The Coulombic efficiency of the cell with 3D Cu anode is ≈99.4% upon 100 cycles, showing high promise for practical applications.

3. Conclusion

In conclusion, we have reported a facile and scalable electrodeposition-dealloying method to fabricate 3D porous Cu structure and its capability of Li-storage and dendrite suppression. The 3D Cu current collector can bear Li storage areal capacity of 10 mAh cm^{-2} and deliver stable cycling performance.

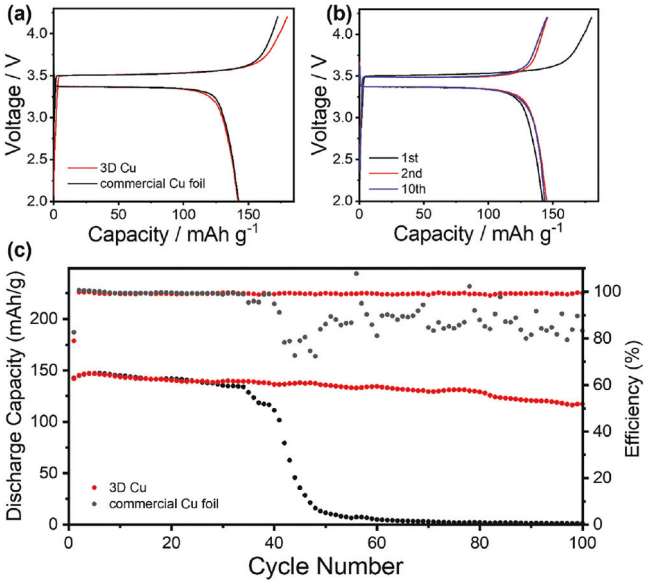

Figure 5. a) Charge/discharge profiles of the full cells with 3D Cu and commercial Cu foil current collectors in the 1st cycle and b) with 3D Cu in 1st, 2nd, and 10th cycle, respectively. c) Cycling performance and CE of full cells with 3D Cu and commercial Cu foil cells at 1C.

Full cell tests with LFP commercial electrodes also show good electrochemical performances and demonstrate its promise as commercial current collectors. Moreover, the as-synthesized porous Cu structure is well combined with commercial Cu substrate and scalable for industrial production. This method can be used to fabricate porous structures owing both high thickness and porosity. Besides, synchrotron XRD results have well revealed phase growth/transformation process during electrochemical deposition/dealloying, providing a deeper understanding of electrodeposition and dealloying process.

4. Experimental Section

Preparation of 3D Porous Cu: The 3D Cu samples were fabricated by first depositing Cn-Zn alloy on Cu foil made for commercial LIBs and then electrochemically dealloying Zn from Cu-Zn alloy. The deposition and dealloying processes were both conducted with using a two-electrode system controlled by a LANHE potentiostat. In deposition, commercial Cu foil (3×3 cm^2) with thickness of 0.0005 in. (MTI Corp.) was used as the substrate and the working electrode, with backside covered with Kapton tape. A Pt foil (2×3 cm^2) was used as the counter electrode. The electrolyte consists of 0.03 M $CuSO_4 \cdot 5H_2O$ (>99.0%, Sigma-Aldrich), 0.5 M $ZnSO_4$ (99.0-103.0% ACS, Alfa Aesar), and 0.25 M $Na_3C_6H_5O_7 \cdot 2H_2O$ (>99.0%, Sigma-Aldrich). Before electrodeposition, Cu substrate was immersed into 0.1 M HCl for 20 s and then rinsed with distilled water to remove the oxide layer on surface. Electrodeposition was conducted in galvanostatic mode with a constant current of 5 mA cm^{-2} for 1 h. Then the sample was taken out, rinsed with distilled water to remove extra electrolyte, and dried in oven at 60 °C before following characterization and tests. In the dealloying process, potentiostatic mode was used. A constant voltage of 0.4 V between the as-deposited Cu working electrode and a piece of Ni foam (3×4 cm^2, >99.99%, 1.6 mm, MTI Corp.) as the counter electrode, in a 0.2 M NaCl (99.5%, OmniPur, MilliporeSigma) aqueous electrolyte for 3 h. After dealloying, the sample was rinsed with distilled water and dried in oven at 60 °C overnight.

XRD and SEM Characterization: In situ and ex situ X-ray diffraction (XRD) measurements were performed to investigate the phase evolution in the deposition and dealloying processes. Ex situ measurements were conducted with using a D8 Advance Diffractometer (Bruker AXS) equipped with a molybdenum radiation source (λ Kα1 = 0.7093 Å). In situ synchrotron XRD data was collected at beam line 28-ID-2 at the National Synchrotron Light Source II (NSLS II) at Brookhaven National Laboratory and beam line 17-BM-B at the Advanced Photon Source (APS) at Argonne National Laboratory. The morphology and microstructure of the deposited/dealloyed samples were investigated with using a high-resolution scanning electron microscope (HR-SEM) (Hitachi SU8230).

Electrochemical Measurements: Electrochemical performances of as-prepared 3D Cu current collectors were tested in standard CR2016 coin cells, assembled in an Ar-filled glove box. The electrolyte consists of 1 M Li-TFSI (Bis(trifluoromethane)sulfonimide lithium salt, 99.95%, Sigma-Aldrich) in DOL/DME (1,3Dioxolane, 99%, Sigma-Aldrich/1,2-Dimethoxyethane, 99.5%, SigmaAldrich) in 1:1 vol. ratio, with 1 wt.% $LiNO_3$ ((>99.0%, Sigma-Aldrich). Li plating/stripping behavior was tested at different current densities in symmetric cells with Li foil (0.25 mm thickness, 3/8 in. diameter) and 3D Cu (7/16 in. diameter) as the two electrodes. Before cycling, all cells were first activated under 50 µA current between 0 and 1 V to remove surface contamination and stabilize solid electrolyte interphase (SEI). For full cell tests, commercial $LiFePO_4$ (LFP, MTI Corp.) was used as cathode. LFP was mixed with carbon black (Super P, MTI Corp.) and Polyvinylidene fluoride (PVDF) (Sigma-Aldrich) with a weight ratio of 8:1:1. The mixture was dispersed into N-methyl pyrrolidone (NMP, J. T. Baker) to form a slurry and then applied onto an Al foil. The LFP electrode film was dried at 100 °C for 24 h in oven. The mass loading of the LFP electrode was controlled ≈2–3 mg cm^{-2}. The 3D current collectors were first cycled in symmetric cells and the amount of Li plated was 1 mAh cm^{-2}. Symmetric cells and full cells were both tested with using a LANHE battery cycler. For comparison, commercial Cu foils were also tested under the same conditions. All reactions and measurements were conducted at room temperature.

Supporting Information

Supporting Information is available from the Wiley Online Library or from the author.

Acknowledgements

The work is in part supported by NSF grants CHE 2108688 and DMR 2004878 and is in part supported by Georgia Tech internal grant. The authors thank beamline scientists at 28-ID-2 of the National Synchrotron Light Source II (NSLS II), 17-BM of the Advanced Photon Source (APS) and BL 7-2 at the Stanford Synchrotron Radiation Lightsource (SSRL) for technical assistance of data collection. This research used resources of the NSLS II, APS, and SSRL, U.S. Department of Energy (DOE) Office of Science User Facilities operated for the DOE Office of Science by Brookhaven National Laboratory under Contract No. DESC0012704, by Argonne National Laboratory under Contract No. DE-AC0206CH11357, and by SLAC National Accelerator Laboratory under contract no. DE-AC02-76SF00515. Y. M. acknowledges support from the China Scholarship Council.

Conflict of Interest

The authors declare no conflict of interest.

Data Availability Statement

The data that support the findings of this study are available from the corresponding author upon reasonable request.

Keywords

current collectors, electrodeposition, in situ X-ray diffraction (XRD), Li-metal batteries, Li storage

Received: February 27, 2023
Revised: April 15, 2023
Published online: May 12, 2023

[1] J. M. Tarascon, M. Armand, *Nature* **2001**, *414*, 359.
[2] B. Dunn, H. Kamath, J. M. Tarascon, *Science* **2011**, *334*, 928.
[3] J. Lu, Z. Chen, Z. Ma, F. Pan, L. A. Curtiss, K. Amine, *Nat. Nanotechnol.* **2016**, *11*, 1031.
[4] J. Liu, Z. Bao, Y. Cui, E. J. Dufek, J. B. Goodenough, P. Khalifah, Q. Li, B. Y. Liaw, P. Liu, A. Manthiram, Y. S. Meng, V. R. Subramanian, M. F. Toney, V. V. Viswanathan, M. S. Whittingham, J. Xiao, W. Xu, J. Yang, X. Q. Yang, J. G. Zhang, *Nat. Energy* **2019**, *4*, 180.
[5] A. Kushima, K. P. So, C. Su, P. Bai, N. Kuriyama, T. Maebashi, Y. Fujiwara, M. Z. Bazant, J. Li, *Nano Energy* **2017**, *32*, 271.
[6] W. Xu, J. Wang, F. Ding, X. Chen, E. Nasybutin, Y. Zhang, J.-G. Zhang, *Energy Environ. Sci.* **2014**, *7*, 513.
[7] A. Zhamu, G. Chen, C. Liu, D. Neff, Q. Fang, Z. Yu, W. Ziong, Y. Wang, X. Wang, B. Z. Jang, *Energy Environ. Sci.* **2012**, *5*, 5701.
[8] D. Lin, Y. Liu, Y. Cui, *Nat. Nanotechnol.* **2017**, *12*, 194.
[9] B. Liu, J. G. Zhang, W. Xu, *Joule* **2018**, *2*, 833.
[10] Y. Lu, Z. Tu, L. A. Archer, *Nat. Mater.* **2014**, *13*, 961.
[11] R. Cao, W. Xu, D. Lv, J. Xiao, J. G. Zhang, *Adv. Energy Mater.* **2015**, *5*, 1402273.
[12] W. Y. Li, H. B. Yao, K. Yan, G. Y. Zheng, Z. Liang, Y. M. Chiang, Y. Cui, *Nat. Commun.* **2015**, *6*, 7436.
[13] L. Suo, Y. S. Hu, H. Li, M. Armand, L. Chen, *Nat. Commun.* **2013**, *4*.
[14] J. Qian, W. A. Henderson, W. Xu, P. Bhattacharya, M. Engelhard, O. Borodin, J. G. Zhang, *Nat. Commun.* **2015**, *6*, 6362.
[15] K. Yan, H. W. Lee, T. Gao, G. Zheng, H. Yao, H. Wang, Z. Lu, Y. Zhou, Z. Liang, Z. Liu, S. Chu, Y. Cui, *Nano Lett.* **2014**, *14*, 6016.
[16] G. Zheng, S. W. Lee, Z. Liang, H. W. Lee, K. Yan, H. Yao, H. Wang, W. Li, S. Chu, Y. Cui, *Nat. Nanotechnol.* **2014**, *9*, 618.
[17] C. Huang, J. Xiao, Y. Shao, J. Zheng, W. D. Bennett, D. Lu, L. V. Saraf, M. Engelhard, L. Ji, J. Zhang, X. Li, G. L. Graff, J. Liu, *Nat. Commun.* **2014**, *5*, 3015.
[18] H. Zhang, X. Liao, Y. Guan, Y. Xiang, M. Li, W. Zhang, X. Zhu, H. Ming, L. Lu, J. Qiu, Y. Huang, G. Cao, Y. Yang, L. Mai, Y. Zhao, H. Zhang, *Nat. Commun.* **2018**, *9*, 3729.
[19] S. Choudhury, R. Mangal, A. Agrawal, L. A. Archer, *Nat. Commun.* **2015**, *6*, 10101.
[20] X. X. Zeng, Y. X. Yin, N. W. Li, W. C. Du, Y. G. Guo, L. J. Wan, *J. Am. Chem. Soc.* **2016**, *138*, 15825.
[21] E. Quartarone, P. Mustarelli, *Chem. Soc. Rev.* **2011**, *40*, 2525.
[22] W. Zhou, S. Wang, Y. Li, S. Xin, A. Manthiram, J. B. Goodenough, *J. Am. Chem. Soc.* **2016**, *138*, 9385.
[23] X. Ren, K. Turcheniuk, F. Wang, A. Y. Song, Q. Huang, Y. Xiao, K. Kim, G. Yushin, *Energy Technol.* **2019**, *7*, 1900064.
[24] C. P. Yang, Y. X. Yin, S. F. Zhang, N. W. Li, Y. G. Guo, *Nat. Commun.* **2015**, *6*, 8058.
[25] R. Zhang, X. R. Chen, X. Chen, X. B. Cheng, X. Q. Zhang, C. Yan, Q. Zhang, *Angew Chem Int Ed Engl* **2017**, *56*, 7764.
[26] B. N. Choi, J. Y. Seo, B. Kim, Y. S. Kim, C.-H. Chung, *Appl. Surf. Sci.* **2020**, *506*, 144884.
[27] X. Y. Yue, X. L. Li, W. W. Wang, D. Chen, Q. Q. Qiu, Q. C. Wang, X. J. Wu, Z. W. Fu, Z. Shadike, X. Q. Yang, Y. N. Zhou, *Nano Energy* **2019**, *60*, 257.
[28] H. Qiu, T. Tang, M. Asif, X. Huang, Y. Hou, *Adv. Funct. Mater.* **2019**, *29*, 1808468.
[29] H. Liu, E. Wang, Q. Zhang, Y. Ren, X. Guo, L. Wang, G. Li, H. Yu, *Energy Storage Mater.* **2019**, *17*, 253.
[30] R. Zhang, S. Wen, N. Wang, K. Qin, E. Liu, C. Shi, N. Zhao, *Adv. Energy Mater.* **2018**, *8*, 1800914.
[31] S. Liu, A. Wang, Q. Li, J. Wu, K. Chiou, J. Huang, J. Luo, *Joule* **2018**, *2*, 184.
[32] Y. Wang, Z. Wang, D. Lei, W. Lv, Q. Zhao, B. Ni, Y. Liu, B. Li, F. Kang, Y. B. He, *ACS Appl. Mater. Interfaces* **2018**, *10*, 20244.
[33] S. Wu, Z. Zhang, M. Lan, S. Yang, J. Cheng, J. Cai, J. Shen, Y. Zhu, K. Zhang, W. Zhang, *Adv Mater* **2018**, *30*, 1705830.
[34] H. Zhao, D. Lei, Y. B. He, Y. Yuan, Q. Yun, B. Ni, W. Lv, B. Li, Q. H. Yang, F. Kang, J. Lu, *Adv. Energy Mater.* **2018**, *8*, 1800266.
[35] Y. An, H. Fei, G. Zeng, X. Xu, L. Ci, B. Xi, S. Xiong, J. Feng, Y. Qian, *Nano Energy* **2018**, *47*, 503.
[36] Y. Xing, S. Wang, B. Fang, Y. Feng, S. Zhang, *Microporous Mesoporous Mater.* **2018**, *261*, 237.
[37] Y. Xu, B. Yu, Y. Wang, F. Tan, G. Cheng, W. Yang, H. Gao, Z. Zhang, *Electrochim. Acta* **2022**, *435*, 141337.
[38] K. Lin, X. Xu, X. Qin, G. Zhang, M. Liu, F. Lv, Y. Xia, F. Kang, G. Chen, B. Li, *Energy Storage Mater.* **2020**, *26*, 250.
[39] J. Ai, *Int. J. Electrochem. Sci.* **2020**, *15*, 2561.
[40] L. Chen, H. Chen, Z. Wang, X. Gong, X. Chen, M. Wang, S. Jiao, *Chem. Eng. J.* **2019**, *363*, 270.
[41] T. T. Zuo, X. W. Wu, C. P. Yang, Y. X. Yin, H. Ye, N. W. Li, Y. G. Guo, *Adv. Mater.* **2017**, *29*, 1700389.
[42] C. Zhang, W. Lv, G. Zhou, Z. Huang, Y. Zhang, R. Lyu, H. Wu, Q. Yun, F. Kang, Q. H. Yang, *Adv. Energy Mater.* **2018**, *8*, 1703404.
[43] W. Yuan, Z. Qiu, Y. Huang, C. Wang, H. Huang, Y. Yang, X. Zhang, J. Luo, Y. Tang, *Energy Technol.* **2019**, *7*, 1900445.
[44] Q. Song, H. Yan, K. Liu, K. Xie, W. Li, W. Gai, G. Chen, H. Li, C. Shen, Q. Fu, S. Zhang, L. Zhang, B. Wei, *Adv. Energy Mater.* **2018**, *8*, 1800564.
[45] G. Luo, X. Yin, D. Liu, A. Hussain, F. Liu, X. Cai, *ACS Appl. Mater. Interfaces* **2022**, *14*, 33400.
[46] G. Luo, D. Liu, J. Zhao, A. Hussain, W. Raza, Y. Wu, F. Liu, X. Cai, *Small* **2023**, *19*, 2206176.
[47] X. Ma, Z. Liu, H. Chen, *Nano Energy* **2019**, *59*, 500.
[48] Q. Yun, Y. B. He, W. Lv, Y. Zhao, B. Li, F. Kang, Q. H. Yang, *Adv. Mater.* **2016**, *28*, 6932.
[49] C. Shan, Z. Qin, Y. Xie, X. Meng, J. Chen, Y. Chang, R. Zang, L. Wan, Y. Huang, *Carbon* **2023**, *204*, 367.
[50] D. Liu, Y. Wang, T. Tong, G. Luo, J. Shen, X. Cai, *Chem. Eng. J.* **2023**, *451*, 138910.
[51] Z. Qin, Y. Xie, X. Meng, D. Qian, C. Shan, D. Mao, G. He, Z. Zheng, L. Wan, Y. Huang, *Chem. Eng. J.* **2022**, *447*, 137538.
[52] Z. Qin, Y. Xie, X. Meng, D. Qian, D. Mao, X. Ma, C. Shan, J. Chen, L. Wan, Y. Huang, *Energy Storage Mater.* **2022**, *49*, 360.
[53] S. Jiao, X. Ren, R. Cao, M. H. Engelhard, Y. Liu, D. Hu, D. Mei, J. Zheng, W. Zhao, Q. Li, N. Liu, B. D. Adams, C. Ma, J. Liu, J. G. Zhang, W. Xu, *Nat. Energy* **2018**, *3*, 739.
[54] X. Q. Zhang, X. Chen, L. P. Hou, B. Q. Li, X. B. Cheng, J. Q. Huang, Q. Zhang, *ACS Energy Lett.* **2019**, *4*, 411.